Journal of Alloys and Compounds 1050 (2026) 185585

Contents lists available at ScienceDirect

Journal of Alloys and Compounds

journal homepage: www.elsevier.com/locate/jalcom

Multi-scale structural heterogeneity driving magnetic softness in relaxed $Fe_{82}Si_2B_{16}$ amorphous alloys: Pathways to enhanced AC permeability

Yuanfei Cai [a,b], Lei Xie [a], Guangjun Lu [c], Shoujiang Qu [d], Xiao Jin [a], Xing Tong [e], Yaocen Wang [f], Jin Du [b], Ning Lv [b], Fei Lv [g], Juntao Huo [a], Meng Gao [a], Jun-Qiang Wang [a,*], Jun Shen [h], Yan Zhang [a,*]

[a] CAS Key Laboratory of Magnetic Materials and Devices and Zhejiang Province Key Laboratory of Magnetic Materials and Application Technology, Ningbo Institute of Materials Technology and Engineering, Chinese Academy of Sciences, Ningbo 315201, China
[b] School of Mechanical Engineering, Yangzhou Polytechnic University, Yangzhou 225100, China
[c] Tangshan Amorphous Technology Co., Ltd., Tangshan 063000, China
[d] School of Materials Science and Engineering, Tongji University, Shanghai 201804, China
[e] Songshan Lake Materials Laboratory, Dongguan 523808, China
[f] School of Physical Science and Technology, Northwestern Polytechnical University, Xi'an 710072, China
[g] Jiangsu Yizhong CNC Machine Tool Co., Ltd., Yangzhou 225200, China
[h] School of Materials Science and Engineering, Fujian University of Technology, Fuzhou 350118, China

ARTICLE INFO

Keywords:
Soft magnetic materials
Critical state
Structural heterogeneity
And AC magnetic property

ABSTRACT

Amorphous alloys exhibit a rich spectrum of energy states. Precise control of the relaxation state enables a further enhancement of AC soft magnetic properties, thereby improving the high-frequency performance of ferromagnetic amorphous alloys. In the high-M_s $Fe_{82}Si_2B_{16}$ amorphous alloy, we elucidate how multi-scale structural heterogeneity governs magnetic property transitions and enables enhanced AC permeability. Through combined magnetic property measurement system (MPMS), transmission electron microscopy (TEM), atomic force microscope (AFM), and local autocorrelation function (ACF) analysis, we demonstrate that thermal annealing triggers two competing processes: annihilation of excess free volume and structure ordering. Through isothermal annealing at 763 K for 10 min, high-density ordered clusters uniformly nucleated and progressively evolved into interconnected medium-range ordered (MRO) regions (2–5 nm), driving the amorphous alloy into a critical state immediately preceding crystallization onset. These structural changes elevate the spin wave stiffness coefficient (149.6 → 151.8 meV·Å^2) and reduce magnetic moment thermal decay, increasing the room temperature saturation magnetization. The coercivity (H_c) reaches the minimal value of 3.3 A/m at 703 K-10 min condition, and further increases the temperature, the H_c increases from 3.3 A/m to 8.4 A/m due to MRO domain wall pinning. However, the AC relative permeability (μ_r) exhibits a further upward trend. AFM analysis reveals the reduced adhesion force heterogeneity and residual stress, which correlate with permeability enhancement, together with the MRO structure formed. The present work establishes that optimizing the balance between MRO and residual stress relaxation during annealing is the key structural origin for advancing AC performance, providing a roadmap for engineering high-permeability Fe-based amorphous alloys.

1. Introduction

Fe-based amorphous alloys have emerged as indispensable magnetic materials due to their excellent comprehensive soft magnetic properties [1,2]. Those with high saturation magnetization (M_s) typically exhibit positive magnetostriction coefficients, with saturation magnetostriction (λ_s) ranging from 25 to 35 ppm [3–5]. The applications-oriented magnetic properties (coercivity, permeability, and core loss) of amorphous alloys are highly sensitive to microstructural variations, enabling quantitative control through post-processing techniques. The magnetostriction coefficient, as an intrinsic material property, is determined by chemical composition, phase constitution, grain size, crystallographic orientation, and impurity levels [6,7].

The metastable nature of amorphous alloys allows for wide

* Corresponding authors.
E-mail addresses: jqwang@nimte.ac.cn (J.-Q. Wang), yzhang@nimte.ac.cn (Y. Zhang).

https://doi.org/10.1016/j.jallcom.2025.185585
Received 21 August 2025; Received in revised form 10 December 2025; Accepted 12 December 2025
Available online 16 December 2025

structural-property tunability in identical compositions [8–10]. For example, enhanced structural heterogeneity through increased cooling rates [11,12], mechanical property optimization via structural rejuvenation from cryogenic treatment [13], multi-state energy regulation through designed annealing [14–17], and the non-monotonic evolution of structural heterogeneity during isothermal relaxation (initial decrease followed by increase) [18]. Such structural control depends on kinetic transformation processes [19], which are governed by thermal history parameters like cooling rate during fabrication, heating rate during annealing, holding temperature/duration, and subsequent cooling rate. The applications-oriented magnetic properties of ferromagnetic amorphous alloys exhibit pronounced sensitivity to structural transformation. Isothermal relaxation involves a continuous transition from β-relaxation (rapid residual stress release, significantly reducing coercivity) to α-relaxation [20,21]. Shao, L. L. et al. [22] discovered in the FeSiBCCr soft magnetic composite system that regulating the amorphous structure to a critical state just before significant crystallization yields superior soft magnetic properties. When a massive crystal-like orders precipitate in the amorphous matrix, the effective permeability reaches its maximum value, resulting in significantly improved high-frequency performance [23]. Amorphous alloys exhibit a broad spectrum of structure-property modulation windows.

In the $Fe_{82}Si_xB_{18-x}$ system, increasing Si content shifts crystallization behavior from eutectic to primary crystallization modes, with $Fe_{82}Si_2B_{16}$ representing the critical transition point. Based on prior Fe-B binary system studies [24], this transition corresponds to a macroscopic phase change in the amorphous matrix, e.g., from Amor. Fe_3B matrix to a Bernal-type Amor. Fe(Si) matrix. At the transition composition region, the alloy exhibits a melting point minimum and maximum atomic packing density [To be published]. The eutectic composition features reduced liquid-phase energy, lower viscosity, and enhanced atomic cluster formation capability [25,26]. The $Fe_{82}Si_2B_{16}$ composition demonstrates superior glass-forming ability, enabling laboratory-scale production of amorphous ribbons with critical thickness $>$ 65 μm.

This study investigates the evolution of intrinsic magnetic parameters and applications-oriented magnetic properties during structural relaxation in high M_s $Fe_{82}Si_2B_{16}$ amorphous alloys, systematically correlating structural heterogeneity with magnetic performance under different magnetic conditions.

2. Experiment

2.1. Materials preparation

The master alloy with a nominal composition $Fe_{82}Si_2B_{16}$ was prepared by a high-frequency induction melting furnace (VF-HMF100, MAKABE, Co., LTD.), using pure Fe (99.98 mass%), Si (99.99 mass%), and crystalline B (99.5 mass%). Ribbons with a width of ~ 1 mm and a thickness of ~ 20 μm were obtained by a single copper roller melting-quenching method (VF-RQB20, MAKABE, Co., LTD.) under a linear rate of ~ 40 m/s in an Ar atmosphere.

The structure optimization method of the as-cast amorphous ribbons was vacuum annealed in a tube furnace. The amorphous samples were pushed into the tube furnace after reaching the target temperature and water-quenched upon completing the 10 min holding time. The annealing temperature range was 583–883 K with 20 K intervals, and the initial heating rate was ~ 6 K/s. The vacuum annealing furnace and typical heating-cooling temearature curve were list in Figure S1.

2.2. Magnetic properties characterization

The M_s–T curve was examined by a magnetic property measurement system (MPMS-SQUID, Quantum Design) from 5 K to 350 K under an excitation magnetic field of 20 kOe (~1600 kA/m). The ribbon sample was cooled from room temperature to 5 K under zero-field conditions, held for 5 min to stabilize the structure, and then subjected to an external magnetic field while being heated to 350 K at a rate of 0.0833 K/s. The magnetic moment was continuously recorded during the heating process. The hysteresis loops were measured by a vibrating sample magnetometer (VSM, Lake Shore 7410) with a maximum applied field of 20 kOe at room temperature. The mass of samples was measured by using an electronic balance (Mettler XS105DU) with a high accuracy of 0.00001 g, and the density of the master alloy was measured by the Archimedean method.

The coercivity and initial magnetization curves were measured by a *B-H* loop tracer (EXPH-100) under the loop and virgin model, respectively. Before measuring the initial magnetization curve, the sample must undergo alternating current (AC) demagnetization to reduce its remanence to zero. Based on the initial magnetization curve, the direct current (DC) initial permeability (μ_i) and maximum permeability (μ_{max}) values can be obtained.

The soft magnetic material is used in the AC environment, and the AC relative permeability (μ_r) of different annealed samples was measured by an impedance analyzer (Agilent 4294 A) from 1 kHz to 40 MHz at 1 A/m external magnetic field.

2.3. Thermodynamic and structure characterization

The thermal analysis of the as-cast ribbons was conducted by differential scanning calorimetry (DSC, Netzsch 404 C) in a Pt crucible at heating rates from 0.0833 K/s to 0.667 K/s under flowing Ar gas. The macroscopic structure of the as-cast and annealed samples was characterized by X-ray diffraction (XRD) with Cu Kα radiation (Bruker, D8 Advance) in a 2θ range from 20° to 90° at a scanning rate of 4 °/min. The microstructure of the as-cast and annealed samples was detected by transmission electron microscopy (TEM, Tecnai TF20), and the TEM samples were prepared via Ar^+ ion milling by the Gatan 691 precision ion polishing system. The selected-area electron diffraction (SAED) and high-resolution TEM (HRTEM) were adopted for microstructure characterization with an acceleration voltage of 200 kV. The magnetic domain was characterized by magneto-optical Kerr effect (MOKE) microscopy (Zeiss, Evico) on the free surface at room temperature.

The nanoscale structural heterogeneity of the samples was characterized by an atomic force microscope (AFM, Bruker Dimension ICON) in PeakForce Quantitative Nano Mechanics (QNM) mode with a silicon tip (3 nm radius, 40 N/m spring constant). Measurements were performed on fresh as-cast surfaces (200 × 200 nm scanning area, 512 × 512 pixels resolution) after standard sapphire calibration and thermal tuning. Adhesive forces were derived from force curve retraction segments, with detailed methodology available in refs. [27,28].

3. Results

3.1. Thermodynamic analysis

Fig. 1 shows the DSC curves of $Fe_{82}Si_2B_{16}$ samples under different heating rates. As the heating rate decreases, the single crystallization exothermic peak splits into two distinct exothermic peaks. The inset displays the endothermic peak corresponding to the ferromagnetic–paramagnetic transition, i.e., the Curie temperature (T_c). Under a heating rate of 0.667 K/s, T_c is determined to be 622.1 K.

At lower temperatures, prolonged structural relaxation promotes the preferential precipitation of the α-Fe(Si) phase. Under higher heating rates, the structural relaxation time at low temperatures is shortened, delaying the onset of initial crystallization at higher temperatures. In this case, the structural ordering of α-Fe(Si) and Fe_3B clusters proceeds simultaneously, resulting in a single eutectic crystallization peak, and the precipitate of α-Fe(Si) and Fe_3B will be verified by XRD characterization.

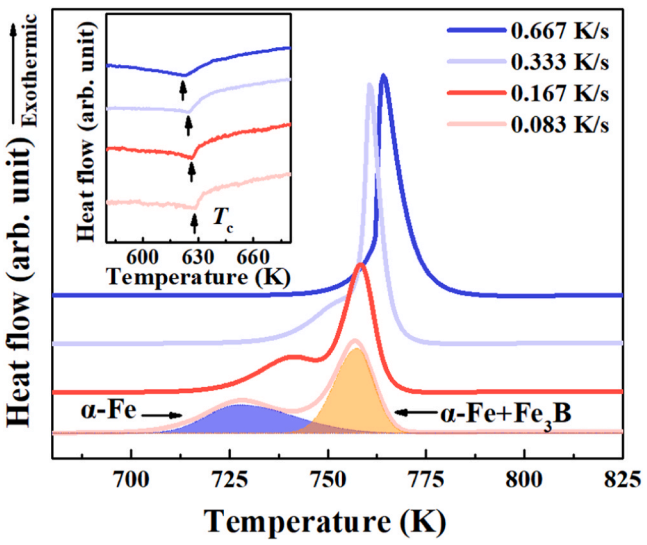

Fig. 1. DSC curves of the $Fe_{82}Si_2B_{16}$ sample under different heating rates, the inset is ferromagnetic–paramagnetic transition, the peak of the curve corresponds to the Curie temperature (T_c).

3.2. Applications-oriented magnetic properties

In practical applications of magnetic materials, applications-oriented magnetic properties (e.g., permeability, coercivity) sometimes hold more immediate relevance than intrinsic magnetic properties (e.g., saturation magnetization, exchange stiffness) [29,30]. These application-oriented magnetic properties directly determine the energy efficiency class of soft magnetic devices during operation and effectively reduce wasteful energy dissipation. Within the framework of the statistical potential theory, the coercivity is determined by several statistically distributed pinning centers [31,32]. While coercivity characterizes DC magnetic response, relative permeability reflects AC behavior, this work demonstrates their fundamentally different structural dependences.

Fig. 2 illustrates the variation of various applications-oriented magnetic properties of $Fe_{82}Si_2B_{16}$ samples as a function of annealing temperature, with detailed numerical data provided in Table S1. In Fig. 2(a), the sample annealed at 703 K for 10 min exhibits the lowest coercivity. Figure S2 shows the coercivity of $Fe_{82}Si_xB_{18-x}$ samples under different annealing temperatures and exhibits a similar tendency. Fig. 2 (b) presents scatter plots showing the dependence of the initial and maximum DC permeability on annealing temperature.

The $Fe_{82}Si_2B_{16}$ samples were vacuum-annealed within the temperature range of 583–883 K, at 20 K intervals, with a holding time of 10 min at each temperature. Table S1 summarizes the corresponding magnetization parameters, including H_c, initial permeability, and AC relative permeability. Under the 703 K–10 min annealing condition, the H_c reaches a minimum of 3.3 A/m, with the corresponding initial permeability approaching its maximum value. However, the relative permeability attains its peak under the 763 K–10 min condition.

In applications involving alternating magnetic fields, the enhancement of relative permeability is of greater practical importance. While it is generally recognized that lower coercivity correlates with higher permeability, coercivity is measured under DC conditions. Therefore,

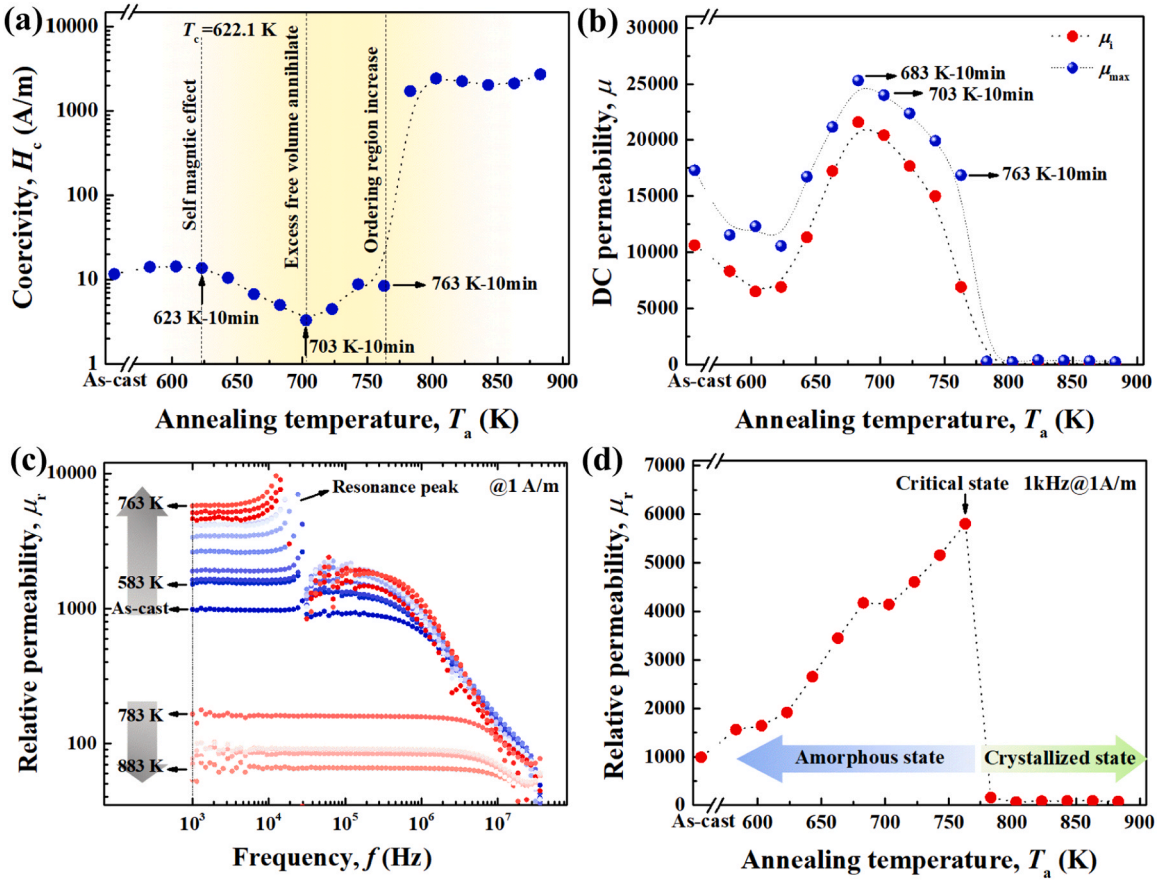

Fig. 2. The applications-oriented magnetic properties of $Fe_{82}Si_2B_{16}$ samples vary with annealing temperature, (a) Coercivity. (b) DC initial permeability and maximum permeability. (c) Relative permeability vs. frequency of different annealing samples. (d) Relative permeability as a function of annealing temperature at 1 kHz frequency.

the optimal annealing conditions for minimizing H_c and maximizing relative permeability differ, reflecting distinct requirements for the amorphous structural state. To address this issue, samples annealed at 603 K, 703 K, 763 K, and 863 K were selected for further characterization of their magnetic properties, structural heterogeneity, and magnetic domain evolution.

During structural relaxation annealing of Fe-based amorphous alloys, the coercivity H_c typically decreases initially, reaching a minimum, and subsequently exhibits a slight increase with further temperature elevation. Upon significant crystallization, H_c deteriorates sharply, resulting in the loss of soft magnetic properties. Fig. 2(c) presents the frequency dependence of the relative permeability under an applied field of 1 A/m. As frequency increases, the relative permeability remains stable up to a critical cutoff frequency, beyond which it declines rapidly. Fig. 2(d) shows the variation of relative permeability at 1 kHz as a function of annealing temperature. With increasing annealing temperature up to 763 K, the relative permeability rises monotonically, followed by a rapid decline to below 100.

An open-ended solenoid was used for the relative permeability measurements, with the calculation performed according to the following formula [33] :

$$\mu_r = \left(\frac{L - L_0}{A_s} + \frac{L_0}{A_0}\right)\frac{l}{N^2\mu_0} \quad (1)$$

In the formula, L_0 represents the inductance of the empty solenoid (H), L is the inductance with the ribbon sample inserted (H), A_0 is the cross-sectional area of the solenoid (mm^2), A_s is the cross-sectional area of the ribbon sample (mm^2), l is the length of the solenoid (mm), and N is the number of turns in the solenoid (180 turns). μ_0 denotes the magnetic permeability of vacuum ($4\pi\times10^{-7}$ H/m).

For magnetostrictive materials with positive magnetostriction, the magnetoelastic energy is proportional to the level of residual stress. The residual stress within magnetic samples significantly affects the mobility of magnetic domains under an alternating field, and the relative permeability is primarily determined by the residual stress level.

3.3. M_s-T curves and XRD analysis

Fig. 3(a) shows the reduced M_s vs. T curves for $Fe_{82}Si_2B_{16}$ samples in different states. As the annealing temperature increases, the decay rate of the magnetic moment with temperature gradually decreases. The reduced M_s vs. T curves were fitted using Bloch's equation [34], with the corresponding expression given as follows:

At low temperatures, the spontaneous magnetization $M_s(T)$ can be described by [24,34] the equation.

$$M_s(T) = M_s(0)(1 - BT^{3/2} - CT^{5/2} - \ldots) \quad (2)$$

The fitting yields the parameters B and C, from which the spin-wave

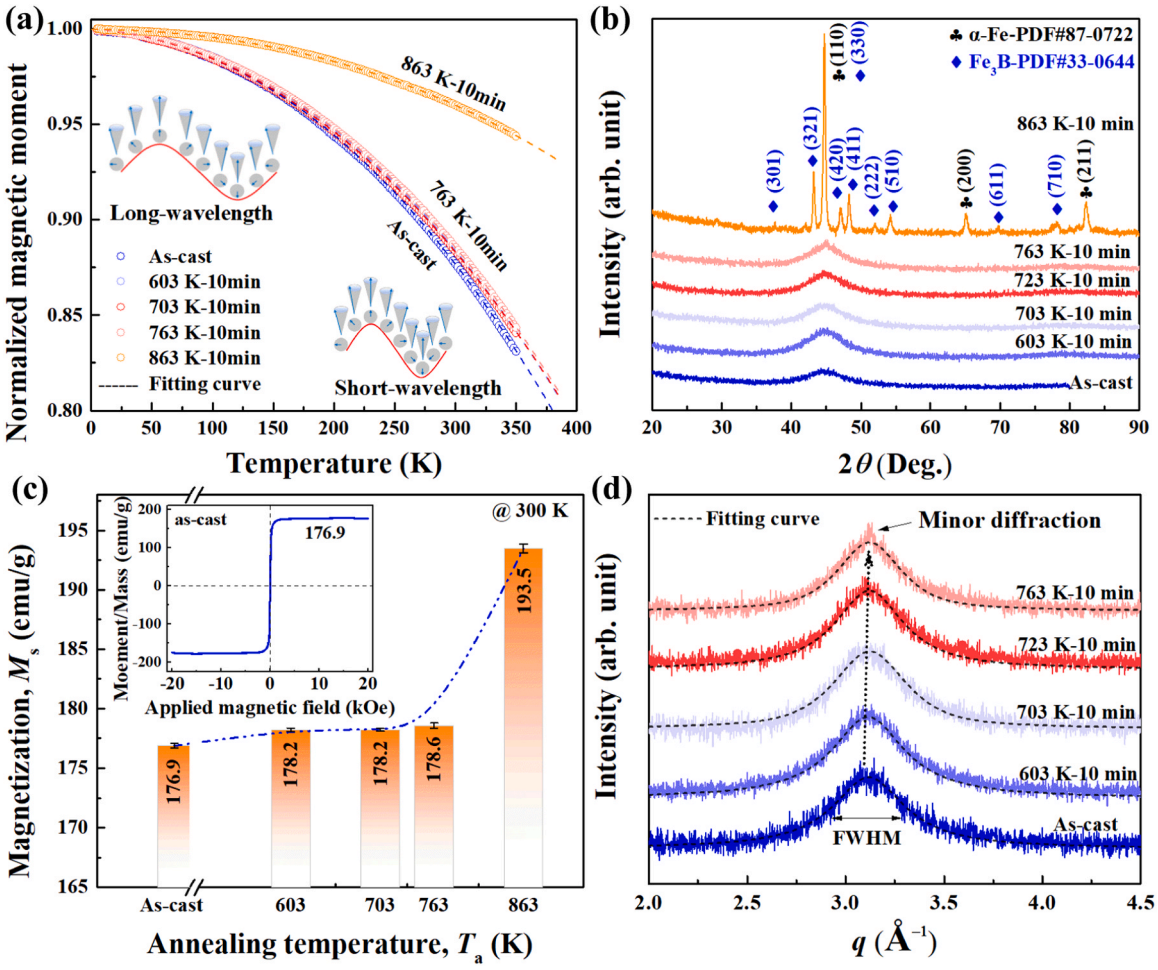

Fig. 3. (a) Normalized magnetization vs. temperature curves for different states of $Fe_{82}Si_2B_{16}$ samples, with an external magnetic field of 20 kOe and a heating rate of 0.0833 K/s. The dash lines are nonlinear fitting curves based on Bloch's equation with goodness of fit $R^2 > 0.99997$. (b) XRD patterns of the free surface of samples in different states. (c) Saturation magnetization as a function of annealing temperature, the inset is the VSM curve of the as-cast sample at 300 K. (d) Fitted image of the broad amorphous diffraction peak in Figure (b), using a Pseudo-Voigt function. The diffraction angle was converted into a spatial vector $\boldsymbol{q}$ using the equation $\boldsymbol{q} = 4\pi\sin\theta/\lambda$, where λ is the Cu Kα X-ray wavelength of 1.54056 Å.

stiffness coefficient D and the exchange interaction range $<r^2>$ are further calculated [35].

$$B = \xi\left(\frac{3}{2}\right)\left(\frac{g\mu_B}{M_s(0)}\right)\left(\frac{k_B}{4\pi D}\right)^{3/2} \quad (3)$$

$$C = \xi\left(\frac{5}{2}\right)\left(\frac{g\mu_B}{M_s(0)}\right)\left(\frac{k_B}{4\pi D}\right)^{5/2}\left(\frac{3}{4}\pi\right)\langle r^2\rangle \quad (4)$$

$$\langle r^2\rangle = \frac{16\xi\left(\frac{3}{2}\right)}{3k_B\xi\left(\frac{5}{2}\right)}\frac{CD}{B} \quad (5)$$

where $\xi\left(\frac{3}{2}\right) = 2.612$ and $\xi\left(\frac{5}{2}\right) = 1.341$ are Riemann zeta functions, k_B is the Boltzmann constant (1.380649×10^{-23} J/K=$8.617333262 \times 10^{-5}$ eV/K), g is the Landé g-factor (taken as 2.1 for Fe-based amorphous alloys), and μ_B is the Bohr magneton (9.2732×10^{-24} J/T). $M_s(0)$ is the extrapolated saturation magnetization at 0 K. Based on these parameters, the exchange stiffness constant A can also be calculated [36].

$$A = \frac{DM_s(0)}{2g\mu_B} = \frac{k_B}{8\pi}\left(\frac{M_s(0)}{g\mu_B}\right)^{1/3}\left(\frac{\xi(3/2)}{B}\right)^{2/3} \quad (6)$$

The intrinsic magnetic parameters of the Fe-based amorphous alloy were obtained based on the M_s vs. T curves, as summarized in Table 1. The exchange stiffness constant A directly reflects the strength of spin-spin interactions within a ferromagnetic material; a larger A value corresponds to stronger interactions between neighboring spins, a greater tendency to maintain parallel spin alignment, and reduced susceptibility to thermal disturbances [37,38]. With increasing annealing temperature, the spin-wave stiffness constant D gradually increases from 149.6 meV·Å^2 in the as-cast state to 151.8 meV·Å^2 after annealing at 763 K for 10 min. Meanwhile, the ferromagnetic exchange coupling length $<r>$ decreases slightly, and the exchange stiffness constant A increases from 1.915×10^{-11} to 1.943×10^{-11} J/m. In the fully crystallized state, the rate of magnetic moment decay is significantly reduced due to the substantial precipitation of α-Fe and Fe_3B phases.

Fig. 3(b) shows the XRD patterns of the free surface of the samples. Up to 763 K, the samples retain a macroscopically amorphous structure. In the sample annealed at 763 K for 10 min, weak diffraction peaks corresponding to ordered structures begin to appear. After annealing at 863 K for 10 min, the sample is fully crystallized, with α-Fe(Si) and metastable Fe_3B identified as the main crystalline phases. Fig. 3(c) presents a histogram showing the variation of saturation magnetization M_s at 300 K as a function of annealing temperature for the $Fe_{82}Si_2B_{16}$ samples. The inset shows the VSM curve of the as-cast sample, with a M_s value of 176.9 emu/g, corresponding to a J_s value of 1.632 T, which is higher than that of $Fe_{78}Si_9B_{13}$ (1.56 T).

A slight increase in the ferromagnetic exchange stiffness constant A is reflected macroscopically by the increase in M_s at 300 K from 176.9 emu/g to 178.6 emu/g. A higher value of A indicates that magnetic moments are less susceptible to thermal disturbances, allowing more residual magnetic moments to align parallel to the external field, thereby leading to higher macroscopic magnetic induction under the same temperature conditions. Stress-relief annealing can therefore slightly enhance the room-temperature M_s of ferromagnetic amorphous alloys. During the structural relaxation process of metastable amorphous alloys, the annihilation of excess free volume occurs [39,40], resulting in a slight increase in density and a decrease in average atomic volume. Annealing also leads to a gradual decrease in the full width at half maximum (FWHM) of the amorphous diffraction peak, from 0.4451 in the as-cast state to 0.3855 after annealing at 763 K for 10 min, indicating an increase in structural ordering. Notably, the increase in structural order does not degrade the intrinsic magnetic properties.

After annealing at 863 K for 10 min, the ferromagnetic exchange stiffness constant increases further, leading to a significant enhancement of the room-temperature $M_s$value. However, the coercivity $H_c$rises sharply to 2726 A/m, and the permeability drops below 100, rendering the material unsuitable for soft magnetic applications and placing it within the category of semi-hard magnetic materials.

3.4. Magnetic domain and B-H loop analysis

The as-cast ribbon samples were prepared by directly quenching the molten alloy. Due to the rapid solidification, a large amount of randomly distributed internal stress is retained within the ribbons. Given the positive magnetostriction coefficient of Fe-based amorphous alloys, randomly oriented stress-induced magnetic domains are formed in the amorphous matrix, as illustrated in Fig. 4(a). In regions under tensile stress, the magnetic domains are broad, whereas under compressive stress, fingerprint-like, fine, and dispersed magnetic domains are observed.

The initial magnetization curve in Fig. 5(d) exhibits two distinct stages, corresponding to domain wall motion and rotation in easily magnetized regions and more difficultly magnetized regions, respectively. When the amorphous sample is annealed below the T_c, it remains ferromagnetic, and randomly distributed magnetic domains persist within the material. During annealing, fine magnetic domains are susceptible to reorientation under the influence of local magnetic fields from wider domain regions, leading to the local ordering and merging of easily magnetized areas, as shown in Fig. 4(b). However, because the annealing temperature is relatively low, the removal of residual stress is limited, increasing macroscopic-induced anisotropy. Consequently, the coercivity does not decrease but instead shows a slight increase.

When the annealing temperature exceeds T_c, the amorphous sample becomes paramagnetic, eliminating the influence of local magnetic fields during structural relaxation. Upon subsequent water quenching, a more uniform domain structure aligned along the easy magnetization direction of the ribbon is formed, where the easy magnetization direction corresponds to the ribbon width, as shown in Fig. 4(c) and Fig. 4(d). Since amorphous alloys lack macroscopic magnetocrystalline anisotropy, their soft magnetic properties are primarily governed by the distribution of short-range order-induced local anisotropies. Under the annealing condition of 703 K for 10 min, the $Fe_{82}Si_2B_{16}$ sample achieved the lowest coercivity of 3.3 A/m. Further increasing the annealing temperature to 763 K results in a gradual rise of the coercivity to 8.4–8.8 A/m. Despite the slight increase in coercivity, the domain

Table 1
The FWHM of the annealed samples and the corresponding spin-wave parameters, including the Bloch constant B and C, the spin-wave stiffness coefficient D, the length of the atomic exchange bond $<r>$, and the ferromagnetic exchange stiffness A.

State	Phase	q (Å^{-1})	FWHM (Å^{-1})	$B \times 10^{-6}$	$C \times 10^{-8}$	D (meV·Å^2)	$<r^2>$ (Å^2)	$<r>$ (Å)	$A \times 10^{-11}$ (J/m)
As-cast	Amor.	3.113	0.4451	1.065	4.297	149.6	72.76	8.530	1.915
603 K	Amor.	3.114	0.4508	1.061	3.873	150.0	65.98	8.123	1.920
703 K	Amor.	3.119	0.4383	1.057	3.923	150.4	67.32	8.205	1.925
763 K	MRO	3.121	0.3855	1.043	3.822	151.8	67.06	8.189	1.943
863 K	α-Fe+Fe_3B			2.778	1.646	366.5	261.8	16.18	4.691

Note: Annealing time: 10 min. Ingot density: 7.503 g/cm^3, estimated amorphous ribbon density: 7.353 g/cm^3.

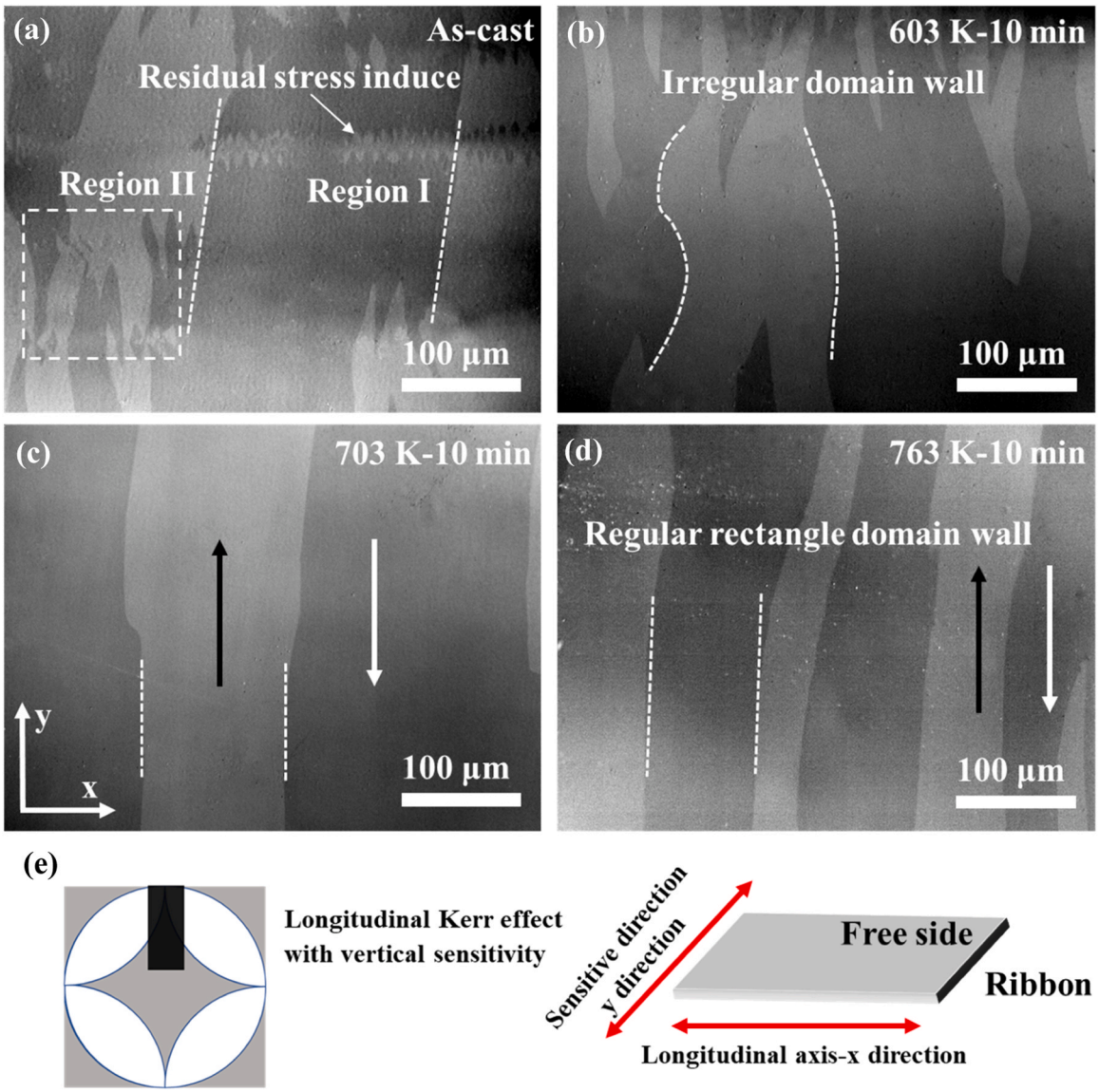

Fig. 4. Magnetic domains of $Fe_{82}Si_2B_{16}$ ribbons under different states on the free side, (a) as-cast. (b) 603 K-10 min annealing state (14.4 A/m). (b) 703 K-10 min annealing state (3.3 A/m). (d) 763 K-10 min annealing state (8.4 A/m). (e) Schematic diagram of longitudinal Magneto-optical Kerr effect aperture and ribbon sample.

structure retains a rectangular pattern, and the relative permeability continues to improve.

Figs. 5(a) and 5(b) present the reduced B–H loops of samples annealed under different conditions. The sample annealed at 703 K for 10 min exhibits the smallest hysteresis loop area, indicated by the red solid line in the figure. Figs. 5(c) and 5(d) show the corresponding initial magnetization curves. The initial permeability first decreases, then increases, and finally decreases again with an increasing annealing temperature, which is inversely correlated with the trend in H_c.

In the as-cast sample, a large amount of residual stress is present, leading to a non-uniform distribution of magnetic domains. The black line in Fig. 5(d) represents the initial magnetization curve of the as-cast sample, which displays two distinct stages: the initial stage (Region I) corresponds to the movement of easily magnetized domain structures. As the external magnetic field increases further, the magnetization curve rises more slowly, with Region II corresponding to the less mobile, wider domain regions. The initial permeability and coercivity of the as-cast sample are primarily influenced by the behavior of Region I. Upon increasing the annealing temperature to 623 K, Region I disappears, and the initial magnetization curve exhibits a single, continuous rise. During this stage, under the influence of stray magnetic fields within the sample, easily movable domains merge and vanish, resulting in a larger random induced anisotropy and leading to an increase in H_c and a decrease in the initial permeability.

3.5. Mesoscale structural heterogeneity analysis

The structural heterogeneity and stress distribution of the selected $Fe_{82}Si_2B_{16}$ samples were further characterized by AFM and TEM. Residual stress leads to the presence of numerous structurally heterogeneous regions within the as-cast ribbon, and AFM offers a reliable method to characterize the distribution of heterogeneity in amorphous alloy ribbons.

Fig. 6**(a)** presents the 3D surface morphology of the as-cast sample, showing atomic-scale surface roughness, with a root-mean-square roughness (R_a) of only 0.0876 nm within a 200 × 200 nm area. Fig. 6 **(b)** displays the corresponding height distribution histogram. Quantitative mechanical testing was performed point-by-point on the sample surface using an AFM probe [27,28], generating two-dimensional adhesion force maps. Fig. 6**(c–e)** illustrate the adhesion force

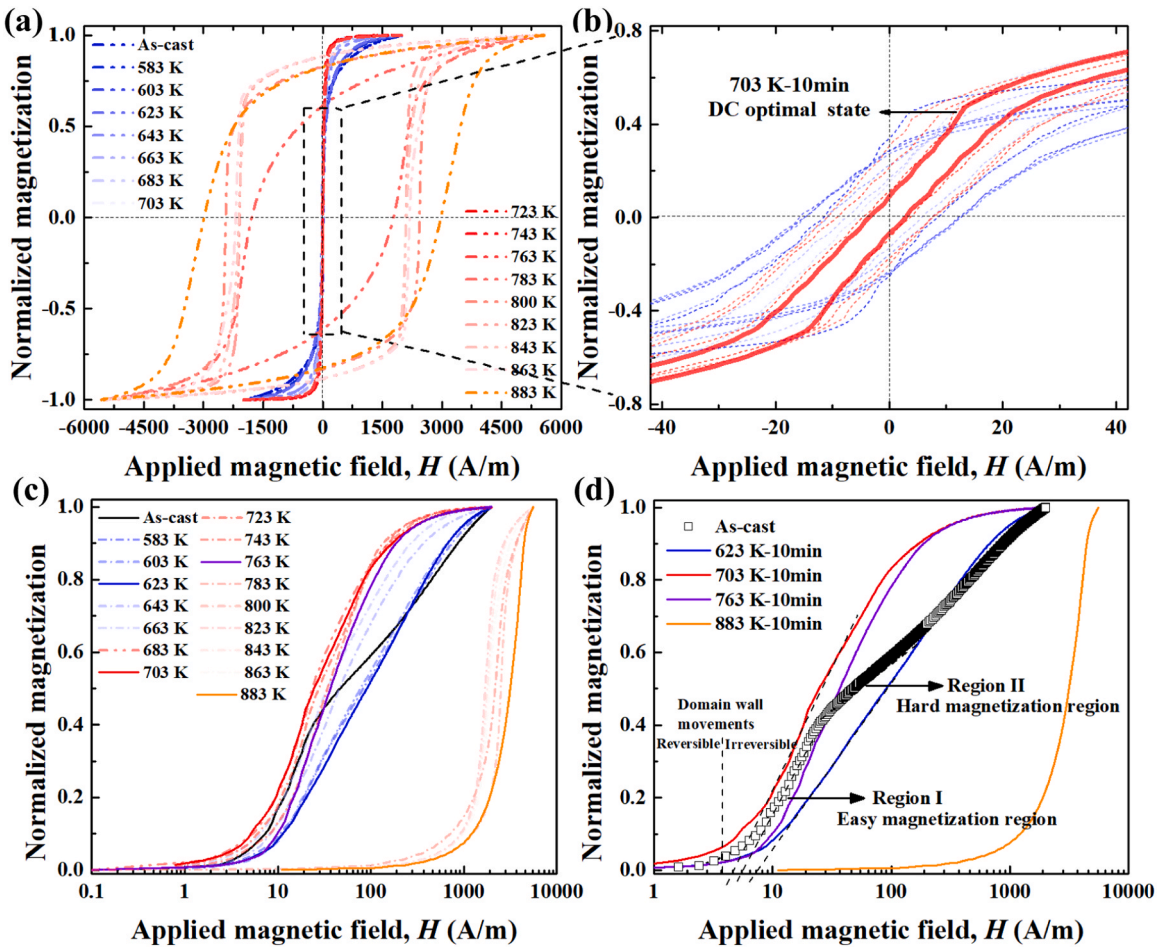

Fig. 5. Variation of $Fe_{82}Si_2B_{16}$ low-field DC hysteresis loop with annealing temperature, (a) DC *B-H* loops at different annealing temperatures. (b) Enlarged view of Figure (a). (c) Initial magnetization curves of samples with different annealing temperatures. (d) Comparative analysis of the initial magnetization curves of typical samples.

distribution maps for the as-cast, 703 K–10 min, and 763 K–10 min samples, respectively, with Fig. 6**(f–h)** showing their corresponding adhesion force histograms. The as-cast sample exhibits the highest degree of adhesion force heterogeneity. In amorphous alloys, regions with higher adhesion forces are termed "liquid-like" regions, while those with lower adhesion forces are referred to as "solid-like" regions [27].

As the annealing temperature increases, the adhesion force heterogeneity within the amorphous matrix gradually diminishes. For the 763 K–10 min sample, the surface adhesion force distribution approaches an unimodal profile, indicating further reduction in heterogeneity compared to the 703 K–10 min sample, and suggesting that the internal residual stresses have been further released. The AC relative permeability increases markedly as domain wall pinning by the heterogeneous structure is progressively mitigated.

3.6. Nanoscale structure ordering analysis

TEM characterization further reveals nanoscale structural evolution during the structural relaxing process. Fig. 7**(a–c)** show the HRTEM images of the as-cast, 703 K–10 min, and 763 K–10 min samples, respectively, with the corresponding SAED patterns displayed as insets. All samples exhibit diffuse amorphous rings at the macroscale. As the annealing temperature increases, local phase-contrast variations emerge within the amorphous matrix, indicating the formation of localized ordered structures. Fig. 8**(a–c)** present the corresponding Fast Fourier transform (FFT) images. In the 763 K–10 min sample, a few sharp ordered diffraction spots, marked by red circles in Fig. 8**(c)**, are observed in the micro-area FFT, while the matrix remains predominantly disordered. These ordered features cannot be directly detected in the larger-area SAED patterns.

To further quantify the local structural order, random 200 × 200 nm regions from the HRTEM images were selected and uniformly divided into 100 squares of 2 × 2 nm each, as shown in Fig. 7**(d–f)**. The local autocorrelation function (ACF) analysis was performed on these subregions, and the corresponding ACF images are displayed in Fig. 7**(g–i)**. When the local ordering scale is comparable to the ACF analysis window, periodic structures emerge, highlighted by red frames in the ACF images. With increasing annealing temperature, the number of localized ordered regions gradually increases. In the 703 K–10 min sample, where H_c reaches its minimum value, excessive free volume is annihilated, residual stresses are reduced, and a small number of localized ordered regions are distributed throughout the matrix. At this stage, the static pinning effect on domain walls is minimized. Upon further annealing at 763 K, structural reordering within the amorphous matrix continues, accompanied by extensive release of residual stress. As shown in Fig. 7**(i)**, the number of ordered regions significantly increases and begins to interconnect, MRO structures spanning 2–5 nm, or localized (meta)stable crystalline nuclei. At this annealing state, a slight increase in H_c is observed, while the AC relative permeability μ_r reaches a maximum value. The homogeneous distribution of MRO is beneficial for further enhancing the soft magnetic properties of Fe-based amorphous alloys under high-frequency AC fields.

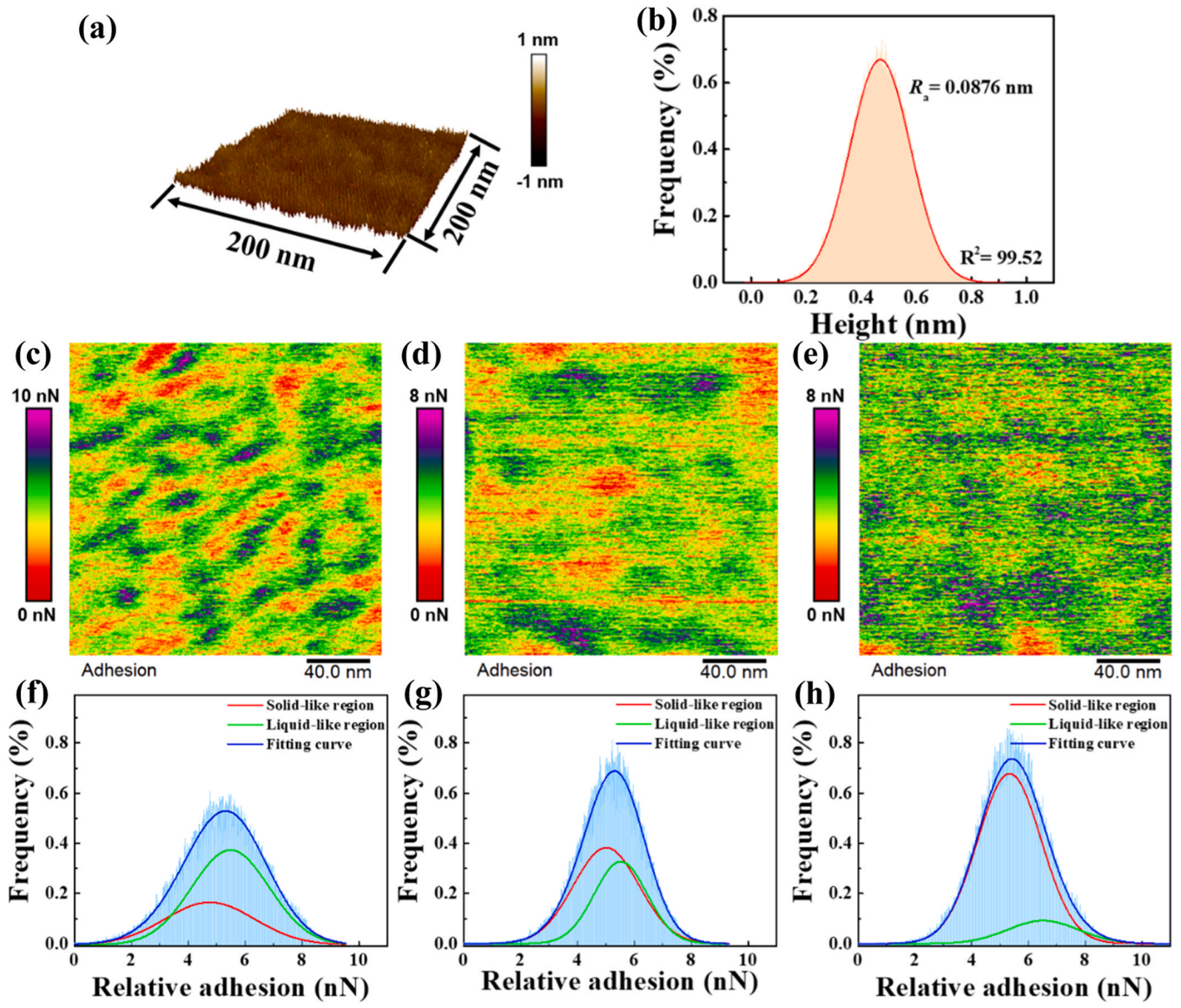

Fig. 6. AFM analysis of typical $Fe_{82}Si_2B_{16}$ samples on the free side, (a) 3D topography of as-cast samples. (b) Frequency distribution of surface roughness. (c) 2D spatial distribution of adhesion of as-cast samples. (d) 2D spatial distribution of adhesion at 703 K-10 min sample. (e) 2D spatial distribution of adhesion at 763 K-10 min sample. (f) Histogram of the frequency distribution of adhesion of as-cast samples. (g) Histogram of the frequency distribution of adhesion in the 703 K-10 min sample. (h) Histogram of the frequency distribution of adhesion in the 763 K-10 min sample. The high-adhesion and low-adhesion regions were fitted by the Gaussian function, which corresponds to the liquid-like and solid-like regions, respectively, and the adhesion is the relative value in the figure.

4. Discussion

An ideal homogeneous and isotropic amorphous alloy should exhibit no macroscopic magnetic anisotropy, yet real materials inevitably deviate from this condition, typically manifesting partial anisotropic energy. The structural heterogeneity in as-cast amorphous alloys originates from nonuniform stress distributions caused by extreme heat transfer from molten liquid to chill copper wheel [41,42]. Fe-based amorphous alloys possess positive magnetostriction coefficients, interacting with residual stresses to induce local magnetic anisotropy, which results in poor coercivity and permeability in the as-cast state, rendering them unsuitable for direct soft magnetic applications. Annealing-induced homogenization of chemical composition and structure significantly reduces macroscopic magnetic anisotropy, thereby improving applications-oriented magnetic properties [43].

The metastable amorphous alloys undergo multiple energy-state transitions during structural relaxation, including annihilation of excess free volume, stress redistribution, MRO rearrangement, and crystalline phase precipitation. The elimination of excess free volume decreases average interatomic spacing, densifies the disordered structure, and increases density [39,44]. This enhances ferromagnetic exchange coupling, evidenced by increased spin-wave stiffness, reduced exchange coupling distance, slower magnetic moment thermal decay, and elevated room-temperature M_s value. When excess free volume is sufficiently released, the ferromagnetic material achieves minimal coercivity. Further increasing the annealing temperature promotes structural ordering, forming localized MRO clusters that weakly pin magnetic domains, slightly increasing coercivity [31,32]. Meanwhile, the AC relative permeability continues rising until crystalline precipitation abruptly degrades it. This structural ordering process reduces adhesion force heterogeneity and the liquid-like region fraction, minimizing local magnetic anisotropy and maximizing relative permeability. The residual stress level critically determines relative permeability. During relaxation annealing, maximizing the annealing temperature without significant crystallization effectively reduces residual stress and forms a high-density MRO structure, thereby optimizing soft magnetic

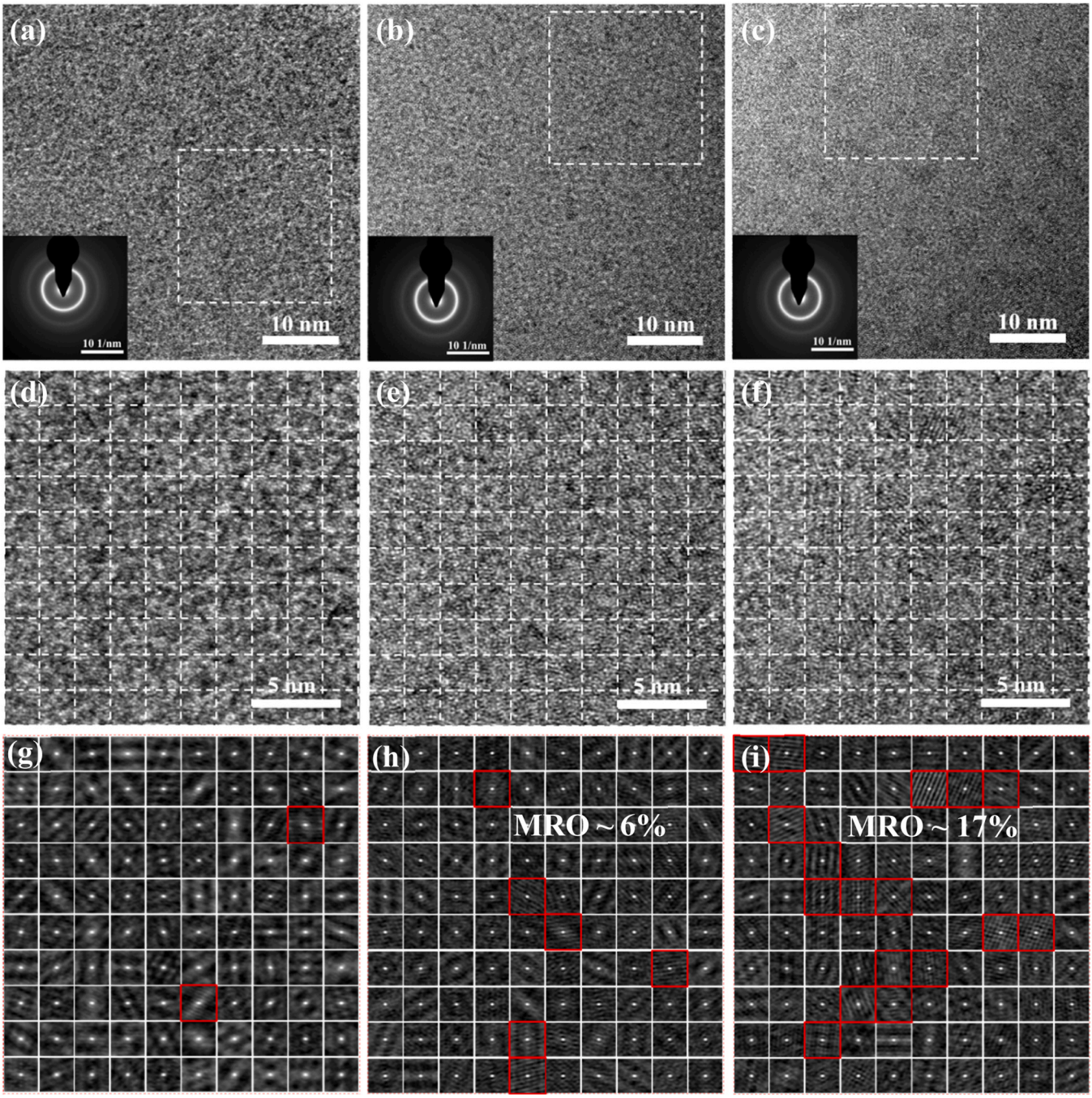

Fig. 7. HRTEM images of $Fe_{82}Si_2B_{16}$ sample under different annealing states, (a) HRTEM of the as-cast sample, inset SAED image of a circular region with a diameter of 785 nm. (b) HRTEM of 703 K-10 min sample, inset as SAED image. (c) HRTEM of 763 K-10 min sample, inset as SAED image. (d) One hundred aliquot images of a randomly selected area of 200 × 200 nm in Figure (a) with a single box of 2 × 2 nm. (e) One hundred aliquot images of a randomly selected region of 200 × 200 nm in Figure (b) with a single box of 2 × 2 nm. (f) One hundred aliquot images of a randomly selected region of 200 × 200 nm in Figure (c) with a single box of 2 × 2 nm. (g) The corresponding ACF image of Figure (d). (h) The corresponding ACF image of Figure (e). (i) The corresponding ACF image of Figure (d), with the red rectangle indicating the ordered regions.

performance under AC conditions.

5. Conclusions

This work establishes a direct correlation between multi-scale structural heterogeneity and magnetic property evolution in relaxed $Fe_{82}Si_2B_{16}$ amorphous alloy, revealing two key pathways to enhanced AC permeability:

As annealing temperature increases, free volume annihilation and structural ordering progress, evidenced by reduced XRD peak FWHM and increased spin-wave stiffness (149.6 → 151.8 meV·Å^2). These changes suppress thermal decay of magnetic moments, elevating room-temperature M_s. Optimal DC soft magnetic property (H_c = 3.3 A/m at 703 K-10 min) arises from balanced stress relaxation and short-range ordering. Further annealing (763 K-10 min) slightly increases H_c (8.4 A/m) but continues to improve AC permeability, demonstrating that the MRO formation (2–5 nm ordered regions) is beneficial to high-frequency performance. AFM-proven reductions in adhesion force heterogeneity and residual stress correlate with diminished "liquid-like" regions, confirming that stress homogenization enhances the domain

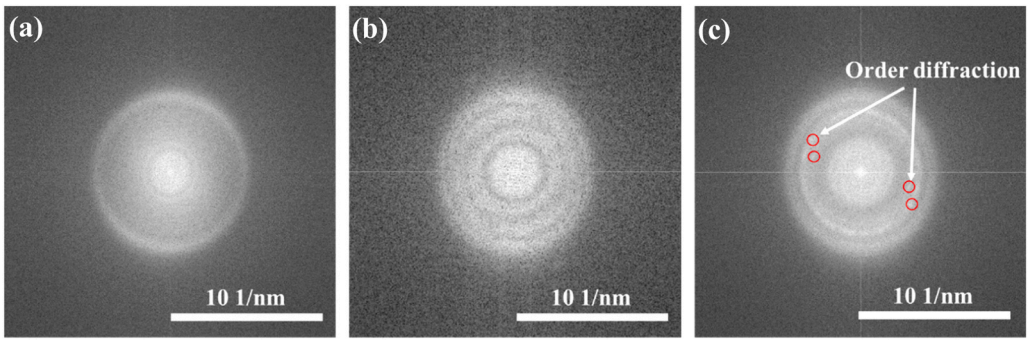

Fig. 8. FFT images of HRTEM of typical $Fe_{82}Si_2B_{16}$ samples, (a) as-cast sample. (b) 703 K-10 min sample. (c) 763 K-10 min sample.

wall mobility under high frequency. Retention of rectangular magnetic domains ensures low hysteresis loss, while interconnected MRO regions provide magnetic homogeneity, synergistically enhancing AC permeability.

CRediT authorship contribution statement

Yuanfei Cai: Writing – original draft, Methodology, Investigation, Data curation. **Lei Xie:** Methodology, Data curation. **Guangjun Lu:** Methodology, Formal analysis. **Shoujiang Qu:** Validation, Supervision, Formal analysis. **Xiao Jin:** Visualization, Methodology. **Xing Tong:** Methodology, Investigation, Data curation. **Yaocen Wang:** Methodology, Investigation, Data curation. **Jin Du:** Visualization, Investigation. **Ning Lv:** Visualization, Supervision. **Fei Lv:** Validation, Methodology. **Juntao Huo:** Supervision, Funding acquisition. **Meng Gao:** Methodology, Investigation, Formal analysis, Data curation. **Jun-Qiang Wang:** Writing – review & editing, Supervision, Project administration, Investigation. **Jun Shen:** Writing – review & editing, Supervision, Resources, Data curation. **Yan Zhang:** Writing – review & editing, Supervision, Funding acquisition.

Declaration of Competing Interest

The authors declare that they have no known competing financial interests or personal relationships that could have appeared to influence the work reported in this paper.

Acknowledgements

This work was supported by the National Key R&D Program of China (Grant No. 2024YFB3813700), the National Natural Science Foundation of China (Grant No. 52301224), the Hebei Natural Science Foundation (Grant No. E2025502090), the Ningbo major R&D Plan Project (Grant No. 2025Z073), the Yangzhou "Green Yangtze Golden Phoenix Plan" (2025) and the High-Level Talent Research Start-Up Project (Grant No. DC2500000934).

Appendix A. Supporting information

Supplementary data associated with this article can be found in the online version at doi:10.1016/j.jallcom.2025.185585.

References

[1] O. Gutfleisch, M.A. Willard, E. Bruck, C.H. Chen, S.G. Sankar, J.P. Liu, Magnetic materials and devices for the 21st century: stronger, lighter, and more energy efficient, Adv. Mater. 23 (2011) 821–842.
[2] J.M. Silveyra, E. Ferrara, D.L. Huber, T.C. Monson, Soft magnetic materials for a sustainable and electrified world, Science 362 (2018) eaao0195.
[3] R.C. O'Handley, M.C. Narasimhan, M.O. Sullivan, Magnetostriction of $Fe_{100-x}B_x$ glasses, J. Appl. Phys. 50 (1979) 1633–1635.
[4] R.C. O'Handley, Magnetostriction of transition-metal-metalloid glasses: temperature dependence, Phys. Rev. B 18 (1978) 930–938.
[5] T. Bitoh, A. Makino, A. Inoue, Origin of low coercivity of Fe-(Al, Ga)-(P, C, B, Si, Ge) bulk glassy alloys, Mater. Trans. 44 (2003) 2020–2024.
[6] K. Sano, T. Yamazaki, R. Morisaki, C. Oka, J. Sakurai, S. Hata, Soft magnetostrictive materials: enhanced magnetostriction of Fe-based nanocrystalline alloys via Ga doping, Scr. Mater. 242 (2024) 115956.
[7] H.D. Huang, H. Tsukahara, A. Kato, K. Ono, K. Suzuki, Effect of magnetostriction on ac initial permeability of amorphous and nanocrystalline alloys, J. Magn. Magn. Mater. 592 (2024) 171810.
[8] Z. Zhang, Z.D. Zhang, Y.F. Cai, Y. Zhang, Y. Wu, H.H. Zhu, Y.Y. Qian, Y.E. Zhang, Y.C. Wang, Y.Q. Yan, X. Tong, B. Zhang, C. Yang, H.B. Ke, H.Y. Bai, W.H. Wang, A unique Fe-based soft magnetic alloy and its magnetic softening mechanism, J. Alloy. Compd. 1002 (2024) 175161.
[9] D.D. Liang, Q. Chen, Y.H. Zhou, X.D. Liu, Y.F. Cai, Q. Zhou, B. Huang, E.G. Zhang, J. Shen, Tailoring the structural heterogeneity and electrochemical behavior of Fe-based bulk metallic glasses by Ar+ irradiation, J. Alloy. Compd. 936 (2023) 168332.
[10] Y.R. Hong, H. Wang, X. Li, L. Zhong, H.M. Chen, Z. Zhang, P.H. Cao, R.O. Ritchie, J.W. Wang, Structural heterogeneity governing deformability of metallic glass, Matter 6 (2023) 1160–1172.
[11] C.B. Jin, Y.Z. Wu, J.N. Wang, F. Han, M.Y. Tan, F.C. Wang, J. Xu, J. Yi, M.C. Li, Y. Zhang, J.T. Huo, J.Q. Wang, M. Gao, Nanoscale viscoelastic transition from solid-like to liquid-like enables ductile deformation in Fe-based metallic glass, J. Mater. Sci. Technol. 194 (2024) 63–74.
[12] Z.Z. Yang, S.S. Jiang, L.X. Ye, C. Zhu, X. Gao, H. Yang, Y.G. Wang, Nanoscale structural heterogeneity perspective on the ameliorated magnetic properties of a Fe-based amorphous alloy with decreasing cooling rate, J. NonCryst. Solids 581 (2022) 121433.
[13] Y.H. Zhu, Y.K. Zhou, A.M. Wang, H. Li, H.M. Fu, H.W. Zhang, H.F. Zhang, Z. W. Zhu, Atomic-scale icosahedral short-range ordering in a rejuvenated Zr-based bulk metallic glass upon deep cryogenic treatment, Mat. Sci. Eng. AStruct. 850 (2022) 143565.
[14] L.J. Song, W. Xu, J.T. Huo, F.S. Li, L.M. Wang, M.D. Ediger, J.Q. Wang, Activation entropy as a key factor controlling the memory effect in glasses, Phys. Rev. Lett. 125 (2020) 135501.
[15] J.Q. Wang, L.J. Song, J.T. Huo, M. Gao, Y. Zhang, Designing Advanced Amorphous/Nanocrystalline Alloys by Controlling the Energy State, Adv. Mater. (2024) 2311406.
[16] B.W. Zang, L.J. Song, R. Parsons, J. Shen, M. Gao, Y. Zhang, J.T. Huo, Y.H. Sun, F. S. Li, K. Suzuki, J.Q. Wang, W.H. Wang, Influence of Thermal History on the Crystallization Behavior of High-B_s Fe-based Amorphous Alloys, Sci. ChinaPhys. Mech. Astron 66 (2023) 256111.
[17] Y.N. Chen, X. Tong, Y.F. Cai, Y.C. Wang, M. Gao, H.B. Ke, G.Q. Zhang, H.Y. Bai, W. H. Wang, J.T. Huo, J.Q. Wang, Y. Zhang, Excellent soft magnetic Fe-based nanocrystalline bulk toroidal cores via one-step low-heating-rate annealing, Sci. ChinaPhys. Mech. Astron 68 (2025) 276111.
[18] Y. Tong, F.C. Li, L.J. Song, Y.H. Liu, J.T. Huo, J.C. Qiao, Y. Yao, J.M. Pelletier, D. Crespo, E. Pineda, J.Q. Wang, Unexpected non-monotonic changing in the heterogeneity of glasses during annealing, J. Mater. Sci. Technol. 177 (2024) 96–102.
[19] W.H. Wang, P. Luo, The dynamic behavior hidden in the long time scale of metallic glasses and its effect on the properties, Acta Matall Sin. 54 (2018) 1479–1489.
[20] N.N. He, L.J. Song, W. Xu, J.T. Huo, J.Q. Wang, R.W. Li, The evolution of relaxation modes during isothermal annealing and its influence on properties of Fe-based metallic glass, J. NonCryst. Solids 509 (2019) 95–98.
[21] Q.H. Xu, L.L. Lu, Q. Yan, F.G. Chen, A. Jain, Y. Lin, H.Z. Zhou, Y.G. Wang, Structural heterogeneity, β relaxation and magnetic properties of Fe-Zr-B amorphous alloys with Si and Cu additions, J. Alloy. Compd. 960 (2023) 171059.
[22] L.L. Shao, R.S. Bai, Y.X. Wu, J. Zhou, X. Tong, H.L. Peng, T. Liang, Z.Z. Li, Q. S. Zeng, B. Zhang, H.B. Ke, W.H. Wang, Critical state-induced emergence of superior magnetic performances in an iron-based amorphous soft magnetic composite, Mater. Futur 3 (2024) 025301.
[23] Y. Wu, W.H. Guo, L.X. Shi, J.L. Jia, R.B. Wang, Y.S. Su, H.T. Bu, Y. Shao, K.F. Yao, Modulation of high-frequency core loss of soft magnetic amorphous alloys through stress release and local structural ordering, J. Mater. Sci. Technol. 256 (2026) 236–245.

[24] Y.F. Cai, B. Lin, Y.C. Wang, R. Umetsu, D.D. Liang, S.J. Qu, Y. Zhang, J.Q. Wang, J. Shen, Relationship among intrinsic magnetic parameters and structure and crucial effect of metastable Fe_3B phase in Fe-metalloid amorphous alloys, J. Mater. Sci. Technol. 180 (2024) 141–149.
[25] H.S. Chen, Glassy metals, Rep. Prog. Phys. 43 (1980) 353–432.
[26] N. Decristofaro, A. Freilich, G. Fish, Formation and magnetic properties of Fe-B-Si metallic glasses, J. Mater. Sci. 17 (1982) 2365–2370.
[27] M. Gao, J.H. Perepezko, Mapping the Viscoelastic Heterogeneity at the Nanoscale in Metallic Glasses by Static Force Spectroscopy, Nano Lett. 20 (2020) 7558–7565.
[28] F. Xu, Y.Z. Liu, X. Sun, J.F. Peng, Y.H. Ding, J.T. Huo, J.Q. Wang, M. Gao, Percolation-like transition from nanoscale structural heterogeneities to shear bands in metallic glass detected by static force microscopy, Appl. Surf. Sci. 611 (2023).
[29] F.E. Luborsky, J.J. Becker, J.L. Walter, H.H. Liebermann, Formation and magnetic properties of Fe-B-Si amorphous alloys, IEEE T. Magn. 15 (1979) 1146–1149.
[30] F.E. Luborsky, P.G. Frischmann, L.A. Johnson, Amorphous materials - A new class of soft magnetic alloys, J. Magn. Magn. Mater. 19 (1980) 130–137.
[31] H. Kronmüller, Theory of the coercive field in amorphous ferromagnetic alloys, J. Magn. Magn. Mater. 24 (1981) 159–167.
[32] H. Kronmüller, Micromagnetism and microstructure of amorphous alloys, J. Appl. Phys. 52 (1981) 1859–1864.
[33] F.Y. Shen, B.W. Zang, L.J. Song, J.T. Huo, Y. Zhang, J.Q. Wang, Ultra-fine microstructure and exceptional low coercivity developed in a high-Bs Fe-Si-B-P alloy by co-alloying Ni, Mo Cu Scr. Mater. 236 (2023) 115666.
[34] S.N. Kaul, P.D. Babu, Detailed magnetization study of quenched random ferromagnets. I. Low-lying magnetic excitations, Phys. Rev. B 50 (1994) 9308–9322.
[35] B.G. Shen, W.S. Zhan, J.G. Zhao, J.C. Chen, Temperature dependence of the magnetization and electrical resistivity for amorphous $Fe_{87-x}Si_xB_{13}$ alloys, Acta Phys. Sin. 34 (1985) 1009–1015.
[36] N.V. Ilin, S.V. Komogortsev, G.S. Kraynova, A.V. Davydenko, I.A. Tkachenko, A. G. Kozlov, V.V. Tkachev, V.S. Plotnikov, Magnetic correlations peculiarities in amorphous Fe-Cu-Nb-Si-B alloy ribbons, J. Magn. Magn. Mater. 541 (2022) 168525.
[37] B.R. Sun, S.W. Xin, T.D. Shen, Low-temperature magnetization and magnetic exchange interactions in $Fe_{40}Ni_{40}P_{14}B_6$ bulk metallic glasses, J. Magn. Magn. Mater. 429 (2017) 276–280.
[38] K. Hüller, The spin wave excitations and the temperature dependence of the magnetization in iron, nickel and their alloys, J. Magn. Magn. Mater. 61 (1986) 347–358.
[39] T. Bitoh, A. Makino, A. Inoue, Magnetization process and coercivity of Fe-(Al, Ga)-(P, C, B, Si) soft magnetic glassy alloys, Mater. Trans. 45 (2004) 1219–1227.
[40] A.R. Yavari, A.Le Moulec, A. Inoue, N. Nishiyama, N. Lupu, E. Matsubara, W. J. Botta, G. Vaughan, M.Di Michiel, A. Kvick, Excess free volume in metallic glasses measured by X-ray diffraction, Acta Mater. 53 (2005) 1611–1619.
[41] J. Zhang, H. Fujimori, A. Inoue, T. Masumoto, Specific heat behaviour on soft magnetic thick amorphous ribbons of an Fe-B-Si alloy, Mater. Sci. Eng. 99 (1988) 35–38.
[42] D. Azuma, R. Hasegawa, S. Saito, M. Takahashi, Effect of residual strain in Fe-based amorphous alloys on field induced magnetic anisotropy and domain structure, J. Appl. Phys. 113 (2013) 17A339.
[43] C.D. Graham, T. Egami, Magnetic properties of amorphous alloys, Ann. Rev. Maler Sci. 8 (1978) 423–457.
[44] G. Haneczok, L. Madej, A. Chrobak, P. Kwapulinski, Z. Stoklosa, J. Rasek, Influence of free volume on magnetoelastic coupling in iron-based amorphous alloys, Phys. Scr. 81 (2010) 5.